atmosphere

Article

Sentinel-2-Based Monitoring and Projection of Lake Burdur Shrinkage in a Climate-Sensitive Semi-Arid Agricultural Basin Using Centroid Kinematics and Robust Trend Modeling

Muzaffer Göztaş [1,*], Nida Oruç Ünal [2], Doğan Yıldız [1] and Dursun Yıldız [3]

[1] Department of Statistics, Faculty of Arts and Sciences, Yıldız Technical University, Istanbul 34000, Türkiye; dyildiz@yildiz.edu.tr
[2] Department of Management Information Systems, Faculty of Economics, Administrative and Social Sciences, Istanbul Topkapi University, Istanbul 34000, Türkiye; nidaoruc@topkapi.edu.tr
[3] Hidropolitik Akademi, Istanbul 34000, Türkiye; dursunyildiz001@gmail.com
* Correspondence: muzaffer.goztas@yildiz.edu.tr

Abstract

In this study, changes in the surface area of Lake Burdur during the 2015–2025 period and the spatial direction of the associated shrinkage were examined using Sentinel-2 Level-2A satellite images. A total of 111 satellite images, each representing a monthly period, were analyzed using a fixed study window and a lake vicinity mask; a three-cluster unsupervised K-means segmentation method was applied to separate the water surface from bare/drained areas and vegetation classes. The resulting binary water masks were used to convert the lake surface area to km^2 on a pixel-by-pixel basis, and the geometric center of the lake mass was calculated for each observation date. The unique aspect of this study is that it evaluates lake shrinkage not only through a decrease in surface area but also as a directional spatial process via the movement of the centroid center. In this context, the cumulative displacement was decomposed into X/West and Y/South components using the initial centroid point as a reference; OLS-based linear and logarithmic trend models were established for both directions. Model performances were compared using a 15-fold Monte Carlo cross-validation approach with R^2, adjusted R^2, NSE, KGE, MAE, MAPE, MSE, and RMSE metrics; additionally, the statistical significance of model differences was assessed using the Wilcoxon signed-rank test. The findings indicate that the logarithmic model yields more balanced and reliable results in the X/West direction, while the linear model does so in the Y/South direction. Based on this model structure, spatial projections were generated for the 2026–2035 period, and it was observed that the projection bands remained stable despite Monte Carlo-based coefficient uncertainty. In conclusion, the study demonstrates that lake drawdowns in semi-arid closed basins can be monitored in a more interpretable and statistically robust manner using Sentinel-2-based segmentation, centroid kinematics, and cross-validated trend modeling.

Keywords: Lake Burdur; Sentinel-2; lake surface area; centroid kinematics; K-means segmentation; Monte Carlo cross-validation; OLS trend model

Academic Editors: Chuan Jin, Guojiao Yang and Licong Dai

Received: 17 June 2026
Revised: 18 July 2026
Accepted: 20 July 2026
Published: 23 July 2026

1. Introduction

Water bodies (lakes, reservoirs, wetlands, etc.) are among the most critical natural resources sustaining ecosystems and human communities. Changes observed in these water basins—whether shrinking or expanding—have increasingly become a significant global concern in recent years. Satellite-based global analyses show that surface water distribution is extremely dynamic. Between 1984 and 2015, approximately 90,000 km^2 of permanent surface water was lost, while approximately 184,000 km^2 of new permanent water surface was formed in other regions [1]. Although a significant portion of this net increase is associated with dam/reservoir construction and climate-induced glacier melt, dramatic losses have been observed in many regions [1,2]. One of the most striking examples of this trend is the Aral Sea in Central Asia, which has lost approximately 87–88% of its surface area since the 1960s [3]. These large-scale declines in large lakes reinforce the need to monitor changes in water bodies and analyze their causes, as these changes have profound consequences on ecological functions and socio-economic systems.

The literature shows that changes in water body areas are mostly shaped by the combination of climate variability and human impacts (water withdrawals, infrastructure, land use). For example, the rapid decline in Lake Urmia, which has a semi-arid closed-basin character, has been discussed in the context of a risk similar to the "Aral syndrome", due to the combined effects of drought, damming, and excessive water use for irrigation [4]. In contrast, the rapid growth of glacial lakes in high mountain ranges since 1990 has been reported in relation to warming and hydrometeorological regime shifts [5]. The fundamental prerequisite for monitoring such area changes in a long-term and consistent manner is a high-resolution and continuous observation infrastructure; modern missions such as Sentinel-2 provide a powerful data source for this purpose at an operational scale [6]. On the other hand, monitoring only the extent of the area does not always explain spatially in which direction the retreat/growth is concentrated. Therefore, recent studies summarize asymmetric retreat–growth patterns as direction-distance vectors by using the movement of the geometric center (centroid/"center of gravity") of the water mass over time and relating them to driving factors [7–9].

However, two key gaps stand out, particularly in the context of semi-arid closed basins. (i) While numerous studies have successfully mapped surface water areas at the global/regional scale [1,2], centroid kinematics, which presents directional shrink-grow dynamics as a compact and interpretable indicator, is more limited and often addressed at a secondary level [8–10]. (ii) Decisions regarding the temporal trend form (e.g., linear vs. logarithmic response) are often reported based on a single fit/single division, and robustness to sampling uncertainty is not sufficiently tested. Considering the increasing role of long-term remote sensing series (e.g., with multiple sensors and derived indicators) in explaining water body changes [10], addressing these two gaps together becomes methodologically critical. This study derives lake surface area (LSA) from monthly Sentinel-2 L2A images for the period 2015–2025 using fixed lake-proximity masking and fully unsupervised segmentation; tracks the geometric center of the LSA mask in a two-component (X-Y; West–South directions) frame; and evaluates OLS-linear and OLS-logarithmic trend forms under Monte Carlo cross-validation (MCCV) and paired statistical comparisons, ultimately transferring coefficient uncertainty to spatial scenario projections for the 2026–2035 period, aiming to directly address these gaps in the literature. Thus, by quantifying the surface footprint of climate–evaporation conditions in a semi-arid closed basin using satellite data, this study also provides a framework for tracking the relationship between atmospheric water demand and lake surface dynamics.

In this context, the original contribution of this study is the first-ever integration of three fundamental components within an end-to-end workflow: (i) centroid kinematics is treated not as a secondary or descriptive indicator, as in previous studies [8–10], but as a

https://doi.org/10.3390/atmos17080710

primary object of analysis representing the direction and magnitude of shrinkage; (ii) the choice between linear and logarithmic trend forms is not based on a single curve fit but is robust against sampling uncertainty through 15-iteration Monte Carlo cross-validation and paired Wilcoxon comparisons; and (iii) the uncertainty in the coefficients associated with the selected model structure is explicitly incorporated into forward-looking spatial scenario projections covering the 2026–2035 period. Furthermore, during the preparation of this study, generative AI tools were used solely for the purposes of improving textual narrative, linguistic editing, and academic expression. Data analysis, methodological design, modeling, interpretation of results, and scientific conclusions were entirely conducted and verified by the author. To the best of our knowledge, this integrated framework—which combines directional centroid tracking with forward-looking spatial projections based on cross-validated model-form selection and uncertainty transfer—has not previously been presented for semi-arid closed-basin lakes; Lake Burdur constitutes the first application of this framework.

2. Materials and Methods

2.1. Related Works

Table 1 summarizes the literature [11–18], presenting a comparative overview of lake/water body dynamics across different continents and basins through the columns source, watershed, country, coordinates, study years, and methods used. For Poyang Lake in China, flood season water area was monitored from 2000 to 2022 using multi-sensor (Landsat-ALOS-Sentinel-1) time series, and area thresholds indicating flood/drought risk were discussed [11]. The spatial evolution of Dongting Lake was examined using multi-source remote sensing from 2005 to 2020; center of gravity (gravity/centroid) migration and driving mechanisms (meteorological–hydrological–human) were evaluated [7]. Similarly, using GEE-based long-term Landsat analyses, area change and center migration in typical plateau and plain lakes in China were correlated with climate variables [12]. In Tonle Sap Lake in the Mekong system, long-term regime change, water level decline, and shoreline retreat were profiled using 2000–2020 hydraulic/remote sensing data together [13]. At Lake Urmia in Iran, comprehensive field measurements and high-resolution images were used to re-examine bathymetric dynamics/area–level–volume relationships, highlighting the success of learning models in bathymetry generation [14]. The shrinkage of Lake Chad in Africa was quantified using Landsat (1987–2005) and interpreted in the context of ecological and socio-economic impacts [15]. In Central Asia, the Aral Basin was monitored using GEE and JRC Global Surface Water from 1992 to 2020, distinguishing between permanent and seasonal water, and a significant decrease in total surface water area was reported [16]. In Aralkum, formed on the drying lake bed, Random Forest-based land cover mapping and uncertainty analysis were performed for 2020 using a combination of Sentinel-1/2 and Landsat-8 [17]. At the city scale in Zhengzhou, the seasonal/long-term patterns of urban water bodies and centroid shift were revealed using Landsat-8 and an integrated Random Forest approach (index + texture) for 2014–2023 [8]. Finally, monthly water extent in Dongting wetlands was mapped at 10 m resolution using Sentinel-1 SAR throughout 2016, allowing detailed differentiation between flood and low-level periods [18].

https://doi.org/10.3390/atmos17080710

Table 1. Summary of related works. (Note: Coordinate values are provided as approximate ranges/centroids for quick comparison; for exact spatial extents, see the original papers.).

Ref.	Country	Water Body	Coordinates	Data and Methods
[11]	China	Poyang Lake (Yangtze River Basin)	28°11′–29°51′ N; 115°49′–116°46′ E	Landsat + ALOS + Sentinel-1; adaptive global-threshold segmentation; flood/drought risk analysis
[7]	China	Dongting Lake (Yangtze River Basin)	28°30′–30°20′ N; 111°40′–113°10′ E	NDWI threshold (multi-season Landsat); center-of-gravity migration; Geographic Detector; correlation analysis
[12]	China	Plateau & plain lakes: Qinghai, Namco, Cuiping, Hengshui	Qinghai: 36°32′–37°15′ N, 99°36′–100°16′ E; Namco: 30°30′–30°35′ N, 90°16′–91°03′ E; Cuiping: 40°00′–40°05′ N, 117°25′–117°40′ E; Hengshui: 37°31–37°41′ N, 115°27′–115°42′ E	Google Earth Engine; Landsat SR; NDWI-based water extraction; shape indices; centroid migration; MLR vs. climate drivers
[13]	Cambodia	Tonle Sap Lake (Mekong River system)	13.02° N, 103.91° E	Multi-source remote sensing + hydrological analysis; shoreline dynamics; attribution to climate & human drivers
[14]	Iran	Lake Urmia (endorheic basin)	37°04′–38°16′ N; 45°02′–46°00′ E	In situ bathymetry + high-resolution satellite imagery; dynamic level–area–volume relationships; bathymetry change analysis
[15]	Chad, Nigeria, Niger, Cameroon	Lake Chad Basin (endorheic)	12°10′–14°30′ N; 13°00′–15°30′ E	Multi-temporal satellite imagery; water-area change detection; socio-economic impact discussion
[16]	Kazakhstan, Uzbekistan, Turkmenistan, Kyrgyzstan, Tajikistan	Aral Sea Basin	36–49° N; 54–74° E	Google Earth Engine; JRC Global Surface Water; seasonal/permanent water extraction; basin-scale trend analysis
[17]	Kazakhstan, Uzbekistan	Aralkum (dried Aral Sea seabed)	43–46° N; 58–62° E	Random Forest; Landsat-8 + Sentinel-2 + Sentinel-1; ten-class LULC mapping; per-pixel uncertainty estimation
[8]	China	Urban water bodies of Zhengzhou (city boundary)	34.75° N, 113.62° E	Landsat 8; thresholding vs. RF vs. hybrid RF (indices + GLCM textures); centroid migration; hotspot analysis; driver analysis
[18]	China	Dongting Lake wetlands	28°30′–30°20′ N; 111°40′–113°10′ E	Sentinel-1 SAR time series; supervised SVM; post-processing to quantify wetland/water dynamics

2.2. Study Area

The study area, Burdur Lake, is a saline-sodic lake with a closed-basin character located in southwestern Turkey, on the northern foothills of the Western Taurus Mountains, between approximately 37.7–37.9° North latitude and 30.0–30.4° East longitude. The semi-arid Mediterranean climate, with hot, dry summers and relatively cool, rainy winters, and the hydrogeological structure represented by carbonate formations and alluvial deposits create a hydrological regime in which the lake is fed mainly by surface runoff, karstic springs, and groundwater, with water losses occurring largely through evaporation and groundwater discharge [19,20]. Increased groundwater withdrawals and agricultural irrigation in recent decades, combined with climate-induced aridification trends, have caused significant decreases in lake level and salinity regime, as well as shoreline retreat, making Lake Burdur a typical example of sensitive semi-arid lake systems [19,20]. Figure 1 shows the lake's location at the global and national scales and the basin boundaries. Additionally, Google Earth-based composites from 30 July 2015, 28 December 2018, 5 February 2022, and 16 November 2025, visually demonstrate the shrinkage of the water body over time. In this study, the lake surface area series derived from the images using Landsat and Sentinel-based approaches is evaluated together with reference evapotranspiration components and additional variables obtained from Open-Meteo data, thus making Lake Burdur an exemplary study area where climatic-evaporation conditions and surface area changes are quantitatively related in semi-arid closed basins [1,21,22].

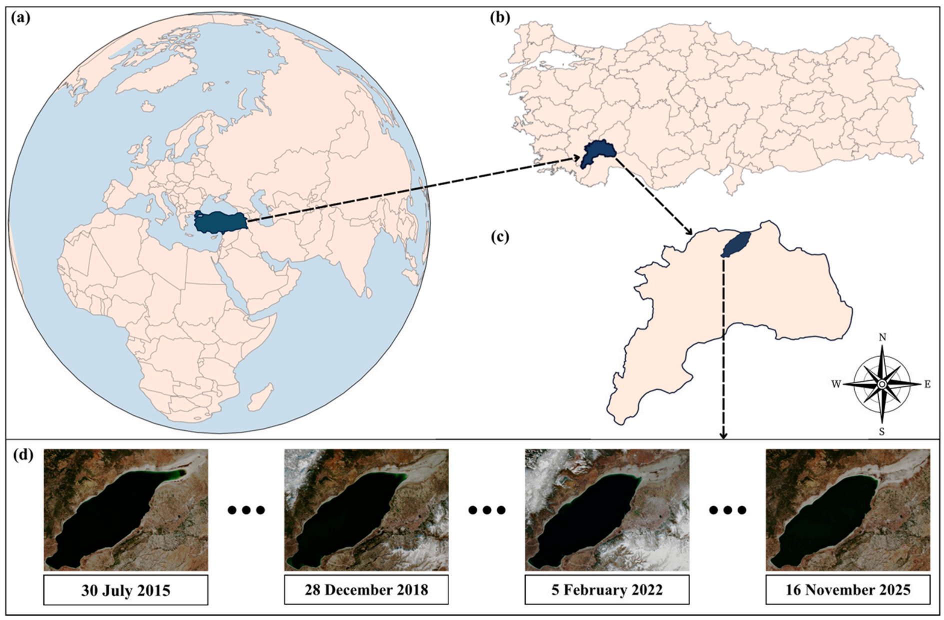

Figure 1. Temporal coverage of satellite images used in the spatial positioning and lake surface area (LSA)-based centroid tracking analysis for the Burdur Lake study area (study area latitude coordinate boundaries: 37°08′–38°02′ North; longitude 29°39′–30°33′ East): (**a**) global scale location, (**b**) Turkey scale location, (**c**) local scale study area boundaries and direction reference, and (**d**) representative examples from selected satellite images between 2015 and 2025.

2.3. Image Processing on LSA

In this study, the temporal change in the surface area of Lake Burdur was calculated using a monthly representative image series generated from fully open-access satellite data. The image source used was the atmospheric-corrected Level-2A products of the Sentinel-2 multispectral optical satellite data provided under the Copernicus program [6]. Since Level-2A products contain spectral bands reduced to surface reflectance, they provide more comparable spectral behavior between different dates. Scenes representing the end of each month were selected for the period 2015–2025; images with a cloud cover ratio below 30% at the scene scale were prioritized, and in some months, the image closest to the end of the month was preferred to maintain the continuity of the time series. This selection strategy resulted in a consistent database of 111 images covering the period July 2015-November 2025, with monthly representativeness preserved (Figure 2, "Database"). To ensure temporal comparability from a geometric perspective, since Sentinel-2 Level-2A products are distributed in a fixed map projection (UTM/WGS84), no additional reprojection was performed; all images were analyzed in their native projection, within the same spatial reference system. In addition, a rectangular working window that remained constant for all dates was defined, and the total working area covered by this window was fixed at A_c= 452.64 km².

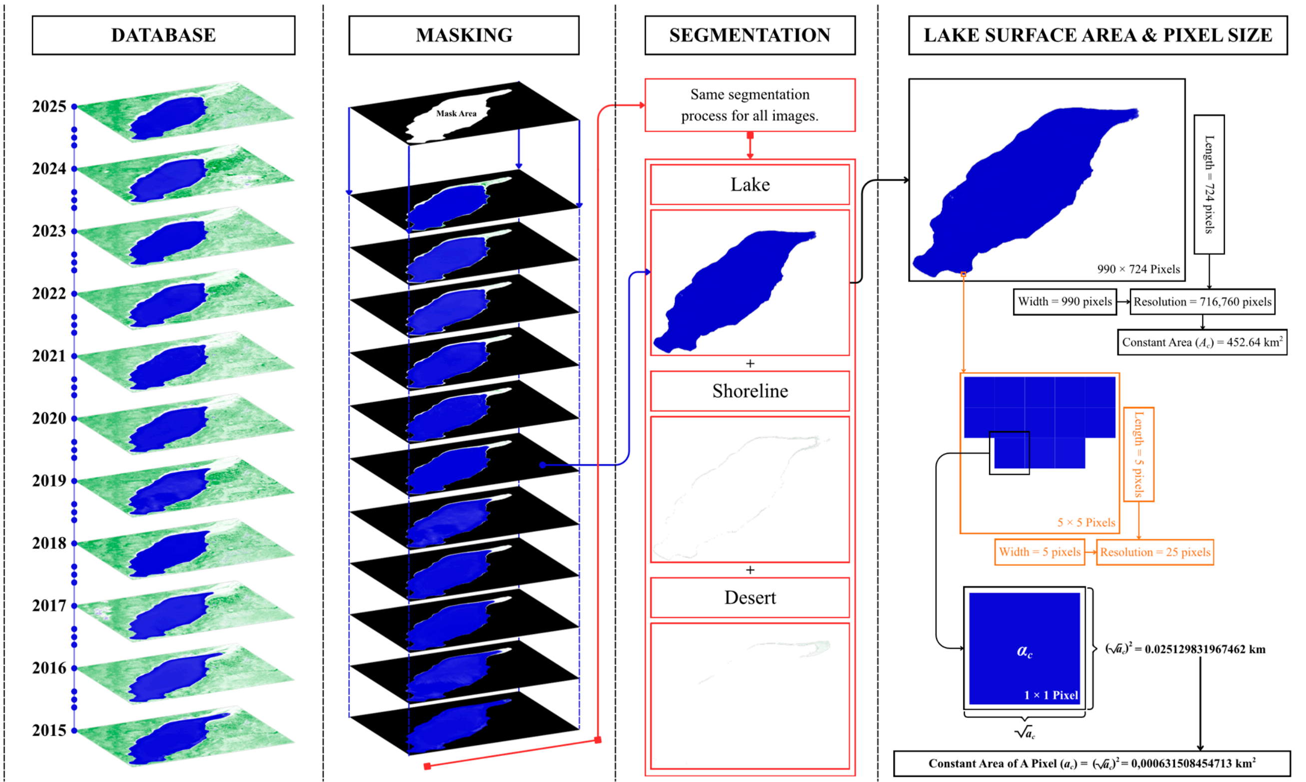

Figure 2. End-to-end satellite image processing workflow for monthly Lake Burdur surface area (LSA) quantification (2015–2025): Copernicus Sentinel-2 Level-2A database construction, fixed lake vicinity masking to reduce misclassification risk, three-class unsupervised K-means segmentation (n_cluster = 3) for lake-shorline-desert, and pixel-based geometric area calibration for consistent LSA retrieval.

In Figure 2 shows that the "Masking" step is designed as a critical control layer in the classification/segmentation process to prevent pixels outside the lake from being incorrectly mixed into the "lake class." In this step, a fixed working mask covering the maximum spread of the lake and its immediate surroundings was applied in the same way for all dates. Pixels outside the mask were set to black with a spectral vector of (0, 0, 0) (Figure 2, "Masking"). Thus, (i) the spatial area included in the analysis was kept constant over time and temporal comparability was preserved, (ii) the clustering algorithm was prevented from being dragged by large land areas far from the lake, which would have distorted the lake class, and segmentation was performed only in the relevant working area.

In Figure 2, under the "Segmentation" step, a multi-band feature space that enhances the water–land separation for pixels remaining within the mask has been defined. Among Sentinel-2's primary bands, Red (R) and Green (G) are in the visible spectrum, while Near Infrared (NIR) has strong discriminating power in distinguishing between vegetation and water surfaces. In practice, a feature vector containing the [R, G, NIR] components for each pixel; additional spectral components/transformations (used in the study) were included in this vector to capture spectral behavior differences more clearly, such as low reflection of water surfaces in NIR and high reflection of vegetation in NIR. Subsequently, the K-means clustering algorithm was used as a completely unsupervised approach [23]. The number of clusters hyperparameter was fixed at n_cluster = 3; initial centers were randomly selected, and solutions were generated for each image until convergence was achieved under a maximum of 300 iterations. The choice of the number of clusters was also supported by AIC and BIC diagnostic plots: in both metrics, the most pronounced decrease occurs in the range k = 1–3; improvements beyond k = 3 are limited, and additional clusters represent nuances in tone and brightness within existing classes rather than new principal surface classes; therefore, k = 3 was chosen while balancing model simplicity and physical interpretability (see Appendix A) [24,25]. The three clusters obtained were interpreted as (i) open water surface (lake), (ii) bare ground/dried lake bed (desert), and (iii) vegetation/agricultural area (green field), considering their spectral characteristics and spatial distribution (Figure 2, "Segmentation"). As a result of this interpretation, the pixel cluster corresponding to the water class was converted to a binary mask format, and a reliable water mask was produced for each month.

The rationale for preferring K-means over common alternatives for water extraction is as follows: NDWI/MNDWI thresholding [26,27] is a robust and widely used approach; however, since the threshold value can vary depending on the scene and season, a 111-date time series requires either the imposition of a single global threshold or the selection of subjective, date-based thresholds-and both scenarios introduce additional uncertainty regarding temporal consistency. Supervised/deep learning approaches such as Random Forest or U-Net, on the other hand, require labeled training data; since a consistent ground truth dataset across dates is not available for Lake Burdur, these methods carry both the cost of generating additional data and the risk of training-set-dependent generalization. In contrast, three-cluster K-means (i) requires no labels since it is entirely unsupervised, (ii) involves no threshold selection and preserves temporal comparability by being applied identically to all dates, and (iii) is computationally lightweight and fully reproducible. The method's limitations are also clear: its performance depends on the spectral resolvability of the bands, the cluster-class mapping involves an interpretation step, and it does not produce probabilistic uncertainty at the pixel level. The practical impact of these limitations has been assessed through the mask-level visual quality control in Appendix C and the cluster-count sensitivity analysis in Appendix A; comparisons between index-based and SCL-based methods at 10 m resolution are left to future studies.

Figure 2 shows the "Lake Surface Area & Pixel Size" step, which defines the conversion of the obtained binary water mask into physical units (km^2) of area. The pixel dimensions of the fixed working window are 990 × 724 resolution, and the actual area represented by this window is A_c = 452.64 km^2. Therefore, the area represented by a single pixel under this window is defined as a_c in Equation (1).

$$a_c = \frac{A_c}{990 \times 724}\ (\mathrm{km}^2/\mathrm{resolution}) \tag{1}$$

Here, α_c is the pixel area coefficient obtained by dividing the fixed window area by the total number of pixels, and it is a constant value for all dates. If the edge length of a pixel is denoted by ℓ and the pixel is known to be square, then the relationship between the pixel area and the edge length is $a_c = \ell^2$, so the edge length can be defined as in Equation (2).

$$\ell = \sqrt{a_c}\ (\mathrm{km}) \tag{2}$$

These two relationships enable the pixel-based count to be linked to the physical scale, and geometric consistency is maintained by performing the conversion using the same scale for each month. Finally, if the number of pixels belonging to the water class for each month is defined as N_{Water}, the lake surface area (LSA) is calculated directly as in Equation (3).

$$LSA = N_{Water} \times a_c\ (\mathrm{km}^2) \tag{3}$$

In Equation (3), N_{Water} represents the total number of pixels classified as "water" in the binary water mask for the relevant month; a_c is the pixel area defined in Equation (1), which remains constant throughout all dates. Under the fixed window and resolution used in this study, as a deterministic result of the fixed window geometry (A_c = 452.64 km^2, 990 × 724 pixels), it takes the value ℓ = 25.13 m (≈0.0251 km). Thus, a monthly LSA time series derived from Sentinel-2 images, converted to physical units at pixel resolution, and geometrically consistent was created.

An explanation regarding pixel size is required. The native band resolution of Sentinel-2 L2A products is 10 m × 10 m; however, in this study, a fixed 990 × 724-pixel analysis grid was created for all dates to ensure computational efficiency and one-to-one geometric comparability across dates, corresponding to a sampling interval of approximately 25 m. Therefore, the value ℓ ≈ 25.13 m reported in Equations (1) and (2) is not the analytical derivation of an unknown parameter, but rather the deterministic result of the fixed window area (A_c = 452.64 km^2) and the grid size is presented solely to verify the internal consistency of the pixel-area transformation. A sampling interval of approximately 25 m provides sufficient spatial resolution for tracking lake area and centroid location at the ~450 km^2 study window scale. However, comparative analyses using a wider set of spectral bands at a native resolution of 10 m, specific water indices (e.g., NDWI/MNDWI) [26,27], and the Scene Classification Layer (SCL; water class code 6) provided in the L2A products will be addressed in future studies.

2.4. Trend Modeling of LSA Centroid Displacement

In this study, the temporal retreat of Lake Burdur has been quantitatively represented through changes in lake surface area (LSA) and the directional displacement of the geometric center (centroid) of the water mask over time. The centroid-based approach allows tracking the dominant direction of lake shrinkage within a two-component kinematic framework; therefore, the analysis is decomposed into a West component along the *X*-axis and a South component along the *Y*-axis. The centroid coordinates obtained at each timestep were converted into cumulative displacement metrics defined relative to the initial center $C_0(x_0, y_0)$, which was referenced from the first image observation.

Decomposition into the X (West) and Y (South) components is a coordinate convention adopted so that displacement can be expressed as positive values, based on the fact that the dominant direction of the observed centroid movement lies in the west–south quadrant; physically, the X component represents the projection of the net retreat along the lake's eastern shores onto the centroid, while the Y component represents the projection of the net retreat along the northern shores onto the centroid. An important point to emphasize here is that the centroid is an integrative geometric indicator: centroid movement combines both shoreline retreat and the asymmetric drying patterns in different sections of the lake into a single vector. For example, a westward shift in the centroid is a result of the shallower areas in the eastern part of the lake drying up faster than those in the western part, and this asymmetry is largely shaped by the bottom topography (bathymetry/hypsometry). Therefore, the direction of centroid movement should not be interpreted as a direct proxy for the spatial direction of hydrological forcing (e.g., wind, river inflow, groundwater withdrawal); rather, it should be evaluated as a diagnostic indicator—along with shoreline geometry and bathymetry—that summarizes where the drawdown is concentrated.

Figure 3 systematically summarizes the referencing logic and cumulative displacement definitions used in the analysis. Figure 3a shows the general distribution of centroid positions obtained on the lake surface during the observation period and the reference centroid position at the starting time t_0. In this panel, the first centroid corresponding to 2015 and the last centroid corresponding to 2025 are presented together, clearly defining the reference point for kinematic change. Figure 3b provides an enlarged view of the region marked in panel (a), making the trajectory followed by the centroid transition points throughout 2015–2025 more distinct. Figure 3c explains the definition of the cumulative displacement components and time difference using a representative example. For each timestep, the cumulative displacement in the X (West) direction is defined as the difference between the X (West) coordinate of the centroid at the relevant date and the X (West) coordinate at time t_0; similarly, the cumulative displacement in the Y (South) direction is defined as the difference in Y (South) coordinates. The time difference is the difference in days between each image date and t_0. Within this framework, consecutive images were overlaid in the same geographic reference system; the displacement between centroids was calculated in the pixel plane and converted to physical length units using image resolution scale information for inclusion in the analysis.

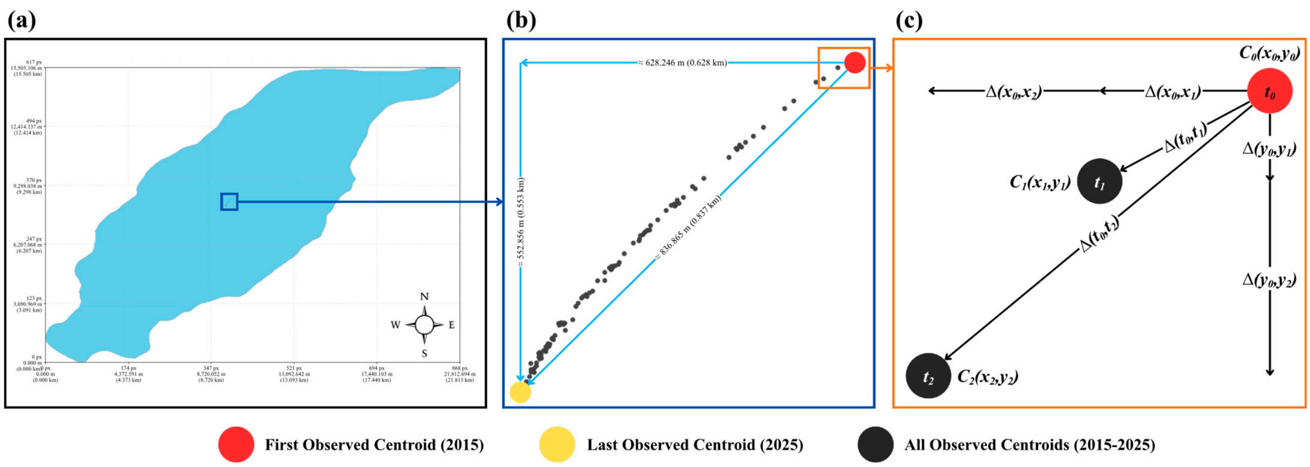

Figure 3. Trend modeling of centroid kinematics in the X (West) and Y (South) direction cumulative displacement framework. (Note: (**a**) Display of the reference initial centroid (t_0) and observed final centroid positions on the lake surface. (**b**) Zoomed-in view of the region marked in the panel (**a**) and a more detailed representation of the centroid transition points. (**c**) Time difference (Δt) component with t_0-referenced cumulative displacement definitions used in trend analysis; for each time point, $\Delta x(t_0,t_n) = x(t_n) - x(t_0)$, $\Delta y(t_0,t_n) = y(t_n) - y(t_0)$, and $\Delta t(t_0,t_n) = t_n - t_0$ (days) calculations.).

After obtaining the centroid displacement series, the functional form of the cumulative displacement curves for both axes was examined using OLS-based regression. The objective at this stage was not to establish a complex family of models requiring parameter search, but to determine the trend form that explains the observed kinematic behavior in the simplest way. Therefore, candidate trends were limited to two classes. The first class (as depicted in Equations (4) and (5)) is a model that expresses cumulative displacement as a linear function of time, assuming that for the X component, Δx is a linear combination of the coefficients β_0 and β_1 with Δt; and for the Y component, Δy is defined under the same structure. The second class (as depicted in Equations (6) and (7)) is based on modeling the cumulative displacement with a logarithmic time transformation. In this model, Δx is defined as a linear combination of the terms β_0 and β_1 with $\ln(1 + \Delta t)$; Δy is defined in the same way via $\ln(1 + \Delta t)$. The use of $1 + \Delta t$ in the logarithmic transformation ensures that the log-term remains defined when $\Delta t = 0$ at the initial reference point and that numerical stability is maintained, stemming from the initial reference point $C_0(x_0,y_0)$ being taken as 0.

$$\Delta x(t_0, t_n) = \beta_{0(x)} + \beta_{1(x)} \Delta t(t_0, t_n) \quad (4)$$

$$\Delta y(t_0, t_n) = \beta_{0(y)} + \beta_{1(y)} \Delta t(t_0, t_n) \tag{5}$$

$$\Delta x(t_0, t_n) = \beta_{0(x)} + \beta_{1(x)} \ln(1 + \Delta t(t_0, t_n)) \tag{6}$$

$$\Delta y(t_0, t_n) = \beta_{0(y)} + \beta_{1(y)} \ln(1 + \Delta t(t_0, t_n)) \tag{7}$$

The selection of the logarithmic form as the candidate trend class is not based solely on statistical fit; it also reflects a hydrological–geomorphological expectation. In closed-basin lakes, as the water level drops, the shoreline first recedes rapidly from wide, shallow shoreline flats; as the level descends into steeper and deeper sections of the lake bed, the change in area (and thus the centroid) corresponding to a unit drop in level gradually decreases. This "fast-then-slowing" behavior, arising from the lake's area–depth (hypsometric) relationship, predicts that the cumulative centroid displacement will follow a curve with a decreasing rate of increase over time (approaching saturation); the $\ln(1 + \Delta t)$ transformation is the simplest functional form representing this type of diminishing-return kinematics with a single parameter. The linear form, on the other hand, corresponds to a scenario where the retreat proceeds at an approximately constant rate; testing both forms together allows for a direction-specific differentiation of which kinematic regime is more consistent with the observed data.

In this part of the study, four OLS models (X-linear, Y-linear, X-logarithmic, Y-logarithmic) were created by defining separate linear and logarithmic trends for the X and Y components (Equations (4)–(7)). The comparison of the models is not based on a single training-validation split; instead, the Monte Carlo cross-validation (MCCV) approach is used [28] to reveal the effect of sampling randomness on the results and to decouple model evaluation from the random properties of a single split. Since the dataset consists of a total of 111 consecutive observation dates, the time difference $\Delta t(t_0,t_n)$ is defined for each tn. Thus, trend modeling was performed using the same time reference without disrupting the sequential structure (date–difference relationship) of the time series. In each MCCV iteration, the training sample was selected from approximately 80–90 observations out of 111 observations; the validation sample was created with approximately 20–30 observations. This selection strategy is critical in two respects: (i) since a different training-validation composition is produced in each iteration, performance metrics are observed in a more robust manner against random sampling variation (ii) since all four models were trained and tested under the same MCCV scheme, intergroup comparisons (especially the linear–logarithmic form difference) were ensured to be conducted under fair and equivalent conditions. This process was repeated over 15 iterations; in each iteration, the equations defined by Equations (4)–(7) were retrained to obtain the coefficients β_0, β_1, and the associated success metrics. Figure 4 schematically summarizes the data flow logic of this MCCV design with data points and how the training/validation samples are resampled in each iteration, how the time order is preserved, and how the four models are compared in parallel (see Figure 4).

The potential impact of applying the MCCV to a temporally ordered series on the assumption of independence in resampling should also be clearly stated here. Cumulative displacement series are, by their very nature, autocorrelated; therefore, randomly selected validation observations are not entirely independent of the training observations, and the reported validation performance should be interpreted as a measure of robustness to sampling variability rather than performance over a "completely unseen period." Three considerations were taken into account to mitigate this effect: (i) since the models contain only deterministic time functions (Δt and $\ln(1 + \Delta t)$), the comparison is less sensitive to autocorrelation than dynamic models that include lagged dependent variables; (ii) since the four models were evaluated in a paired manner on the same training/validation split at each iteration, the effect of autocorrelation on the metrics is largely simplified as a common (shared) component in the model comparison; and (iii) the significance of model differences was tested using the paired Wilcoxon signed-rank test, which does not require a distribution assumption. However, it is known that potential autocorrelation in the residuals may cause the coefficient standard errors to appear smaller than they actually are; therefore, the choice of model form was not based solely on parametric t/F tests; the decision was based primarily on the average behavior of the validation performance observed across MCCV and on paired Wilcoxon comparisons, which do not require assumptions about distribution.

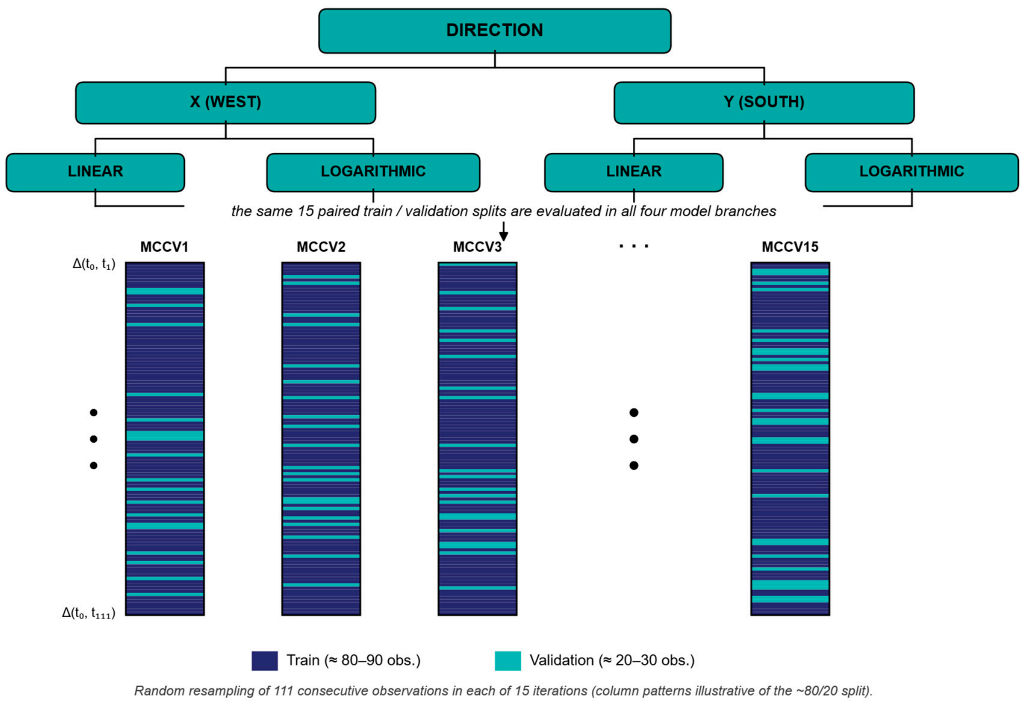

Figure 4. Monte Carlo cross-validation (MCCV, 15 iterations) evaluation scheme designed while preserving the time series: Random resampling of training and validation sets with approximately 80–90 observations for training and 20–30 observations for validation from 111 consecutive observations in each iteration. A common sampling scheme for comparing linear and logarithmic OLS models (Equations (4)–(7)) in the X (West) and Y (South) components under fair and equivalent conditions.

3. Results

3.1. Trend Models' Coefficients and Significances

In this study, two different functional forms (OLS-linear and OLS-logarithmic) were separately established for the cumulative displacement components X (West) and Y (South), which represent the movement directions of Burdur Lake's central position over time; thus, a total of four trend models were obtained. The parameters of each model were repeatedly re-estimated in a 15-step Monte Carlo cross-validation (MCCV) scheme, maintaining the time order. Table 2 reports the values of the β_0 and β_1 coefficients for each model throughout these 15 MCCV steps. Additionally, testing each coefficient with a t-test (H_0: $\beta_i = 0$) and testing the overall significance of each model with an overall F-test (H_0: the model has no explanatory power) demonstrates that the established trend relationships are also statistically supported. According to the findings, significance was maintained at the coefficient level and model level in all four models; the reported *p*-values remaining below 0.001 revealed that the trend structure was produced systematically rather than randomly throughout the MCCV and that the model formulations provided a reliable parametric basis.

Table 2. Coefficient estimates (β_0, β_1) for linear and logarithmic OLS models according to direction components (X-West, Y-South) throughout the Monte Carlo cross-validation (MCCV, n = 15) steps.

MCCV Steps	Coefficients							
	X (West)				Y (South)			
	Linear		Logarithmic		Linear		Logarithmic	
	β_0	β_1	β_0	β_1	β_0	β_1	β_0	β_1
1	0.18231	0.00013	−0.86666	0.17874	0.11116	0.00013	−0.83518	0.16310
2	0.19757	0.00013	−0.96274	0.19147	0.12150	0.00012	−0.94028	0.17699
3	0.18373	0.00013	−0.93889	0.18818	0.11097	0.00013	−0.91102	0.17293
4	0.17724	0.00014	−0.89304	0.18210	0.10651	0.00013	−0.85719	0.16580
5	0.18696	0.00013	−0.88279	0.18088	0.11472	0.00013	−0.85564	0.16581
6	0.18720	0.00013	−0.88111	0.18047	0.11411	0.00013	−0.85580	0.16563
7	0.18245	0.00013	−0.88117	0.18065	0.11161	0.00013	−0.85182	0.16532
8	0.18847	0.00013	−0.99042	0.19496	0.11427	0.00013	−0.95978	0.17930
9	0.20099	0.00013	−0.96089	0.19124	0.12290	0.00012	−0.94674	0.17772
10	0.19623	0.00013	−0.91101	0.18453	0.11988	0.00012	−0.90360	0.17220
11	0.19238	0.00013	−0.85130	0.17680	0.11835	0.00013	−0.82967	0.16233
12	0.18466	0.00013	−0.87937	0.18029	0.11248	0.00013	−0.85561	0.16562
13	0.19761	0.00013	−0.95800	0.19078	0.12132	0.00012	−0.94451	0.17754
14	0.19499	0.00013	−0.85042	0.17675	0.11990	0.00012	−0.83126	0.16275
15	0.18959	0.00013	−0.87956	0.18033	0.11460	0.00013	−0.85354	0.16534

The stability of the coefficients throughout MCCV iterations is as critical as their meaningfulness for the reliability of simulation outputs. To this end, Figure 5 summarizes the β_0 and β_1 coefficients of each model separately using boxplots to observe distributional stability and possible deviations. The absence of outlier values in the panels and the balanced structure of the median-quartile ranges support that the coefficients remained stable throughout the MCCV steps and that the randomness of sampling, performed while preserving the time order, did not distort the parameters. Thus, the consistency of the coefficients seen step-by-step in Table 2 is also confirmed distributionally in Figure 5 (Appendix B shows the same coefficient behavior distributed over 15 MCCV steps based on the model).

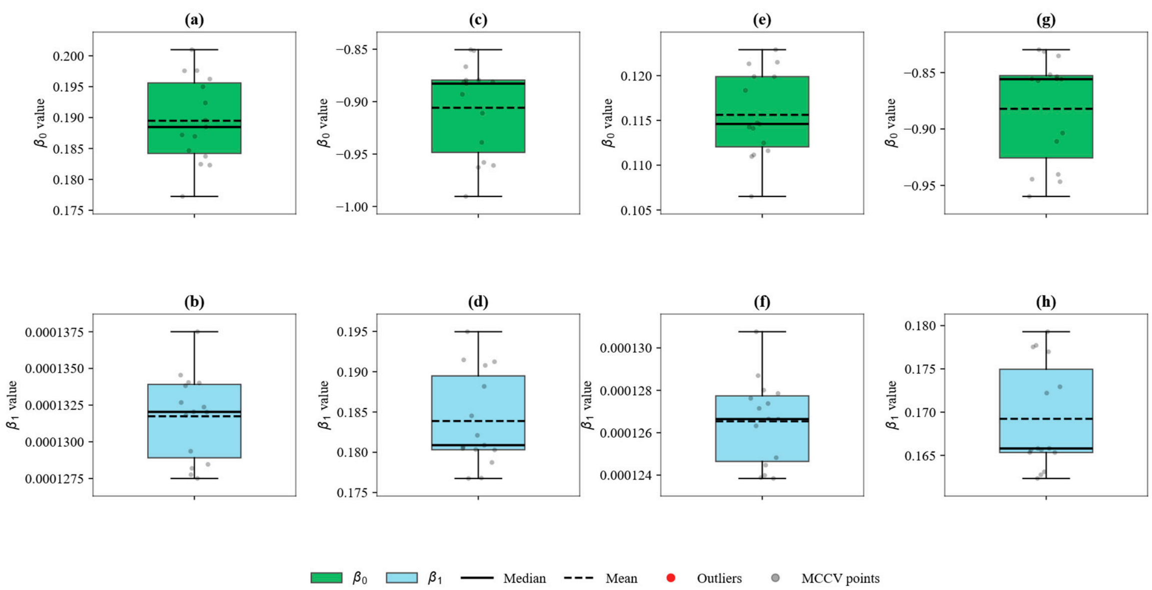

Figure 5. Stability of trend coefficients: Boxplot panels for β_0 and β_1 under MCCV (15 repetitions) (outlier control and internal consistency). (Note: This figure summarizes the distribution of coefficients in eight panels: (**a**) X (West) OLS-linear β_0, (**b**) X (West) OLS-linear β_1, (**c**) X (West) OLS-logarithmic β_0, (**d**) X (West) OLS-logarithmic β_1, (**e**) Y (South) OLS-linear β_0, (**f**) Y (South) OLS-linear β_1, (**g**) Y (South) OLS-logarithmic β_0, and (**h**) Y (South) OLS-logarithmic β_1. The absence of red outlier points in the panels indicates that the coefficients did not deviate to extreme values in any MCCV iteration; the balanced appearance of the median and interquartile ranges indicates that the coefficients exhibited internal consistency across iterations).

3.2. Model Success Metrics' Results

Validation averages in the X (West) direction favor the logarithmic form across all explanatory metrics: 0.948 versus 0.874 for R^2, 0.945 versus 0.868 for Adjusted R^2, and 0.948 versus 0.874 for NSE (logarithmic vs. linear; Figure 6). Error-based metrics also show the same pattern: MAE 0.026 vs. 0.043, MAPE 19.99 vs. 30.07, MSE 0.00110 vs. 0.00273, and RMSE 0.0328 vs. 0.0517. Only in the KGE are the two models nearly equivalent in validation (0.883 vs. 0.882). In the linear model, the training and validation averages are nearly identical (small generalization gap), while in the logarithmic model, a small but controlled decline is observed; however, the absolute validation performance of the logarithmic form is significantly higher in all metrics except KGE.

In the Y (South) direction, however, the picture is reversed: the linear form produces better validation averages for R^2 (0.933 vs. 0.926), Adjusted R^2 (0.930 vs. 0.923), NSE (0.933 vs. 0.926), and particularly in the KGE, which simultaneously accounts for correlation–bias–variance components, it produces better validation averages (0.924 vs. 0.891); for MSE and RMSE, the two forms are practically equivalent (0.001259 vs. 0.001278 and 0.0352 vs. 0.0354). The logarithmic form shows only a limited advantage in MAE (0.0277 vs. 0.0293) and MAPE (23.19 vs. 24.07); however, these small differences are not large enough to reverse the linear form's superiority in explanatory power and balanced fit metrics. Consequently, the logarithmic form was preferred for the X (West) component, and the linear form for the Y (South) component.

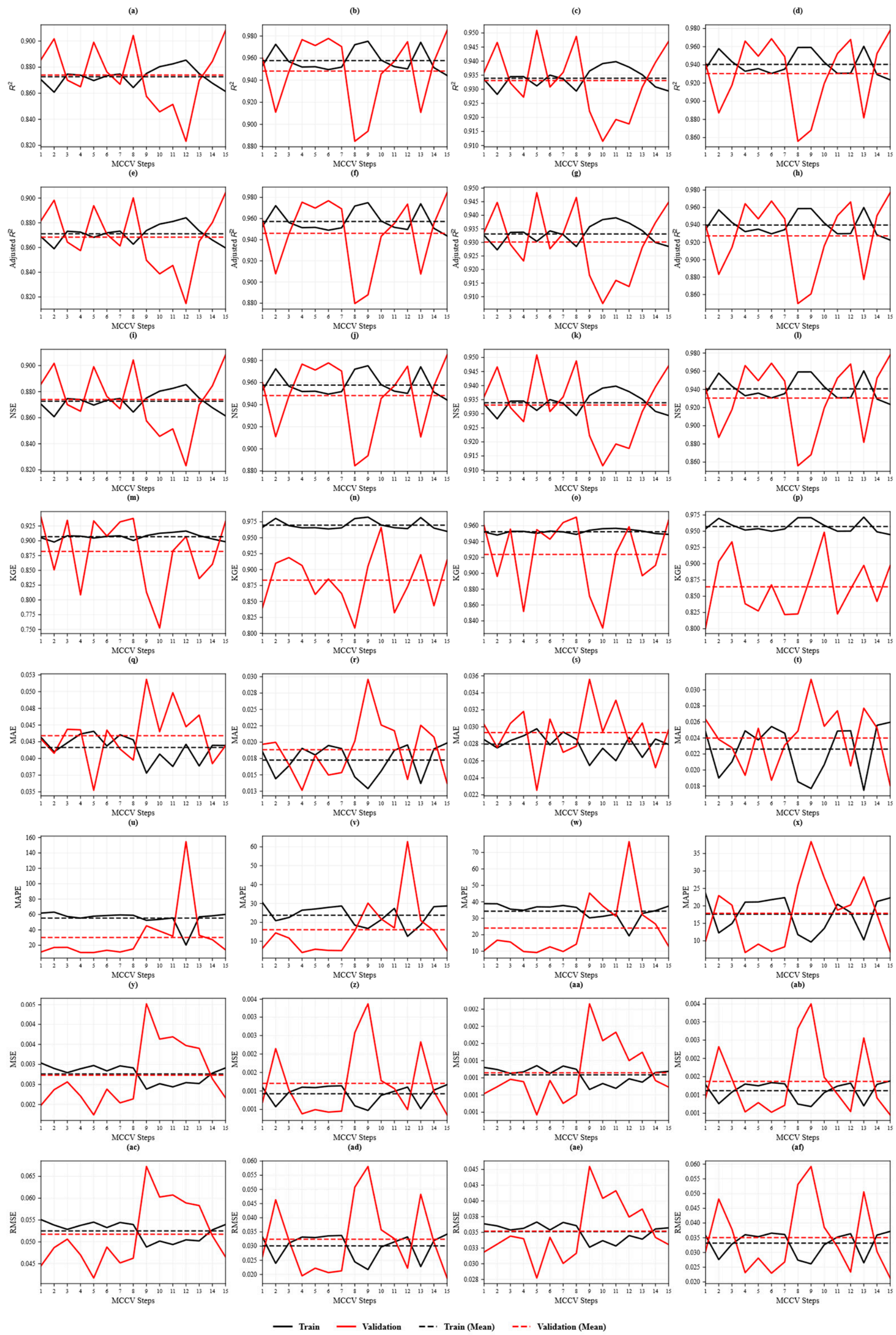

Figure 6. Monte Carlo cross-validation (MCCV, 15 iterations)-based model performance matrices: Comparison of training and validation success metrics for OLS-linear and OLS-logarithmic regressions in the X (West) and Y (South) components of the cumulative displacement of the Burdur Lake LSA centroid. (Note: In Panels (**a**,**e**,**i**,**m**,**q**,**u**,**y**,**ac**) are for OLS-linear in the X (West) direction; (**b**,**f**,**j**,**n**,**r**,**v**,**z**,**ad**) panels present OLS-logarithmic results for the X (West) direction. Similarly, (**c**,**g**,**k**,**o**,**s**,**w**,**aa**,**ae**) panels show OLS-linear results for the Y (South) direction; (**d**,**h**,**l**,**p**,**t**,**x**,**ab**,**af**) panels show OLS-logarithmic results for the Y (South) direction. Each panel presents the train (black solid) and validation (red solid) series along with their means (black dashed and red dashed) over 15 MCCV steps; thus allowing (i) generalization gap (Train-Validation mean difference) and (ii) stability/fluctuation (volatility across MCCV steps) to be visually tracked. In maximization-based

metrics (R^2, Adjusted R^2, NSE, KGE [29,30]), a higher value indicates better fit; in minimization-based metrics (MAE, MAPE, MSE, RMSE), a lower value indicates lower error.).

3.3. Paired Non-Parametric Comparison of OLS Models

The following section demonstrates whether the success metrics produced by the OLS-linear and OLS-logarithmic models over 15 MCCV steps differ statistically significantly, based on the *p*-values from the Wilcoxon signed-rank test (a non-parametric test [31] for paired/dependent samples) reported in the 16 subpanels of Figure 7. Since the MCCV iterations come from the same data generation mechanism and the same iterations are compared at each step, the analyses were conducted in a matched-pairs (paired) design. Furthermore, due to the limitation of the number of iterations to 15 and the possibility that the normality assumption in the metric distributions may not be reliable, the Wilcoxon signed-rank test, which does not require a distribution assumption, was preferred over parametric alternatives (e.g., paired-samples t-test). All hypothesis tests were applied as two-sided (two-tailed); the aim was not to test the superiority of any model in a directional manner, but to assess whether there was a statistically significant difference between the matched metric values. Three main comparisons are reported for each panel: (i) the Train-Validation difference in the linear model (generalization gap/overfitting signal), (ii) the Train-Validation difference in the logarithmic model, and (iii) the Validation difference between models (statistical divergence in validation performance). A significance level of $\alpha = 0.05$ is used in the interpretations.

The overall pattern of the Wilcoxon paired comparisons can be summarized in three findings (Figure 7). (i) Differences in validation performance between models in the X (West) direction are highly significant for all metrics-R^2, Adjusted R^2, NSE, MAE, MAPE, MSE, and RMSE ($p < 0.001$); the sole exception is KGE, where the two models do not differ in validation performance ($p = 0.804$). This result confirms that the logarithmic superiority in the X direction is not random within the MCCV uncertainty. (ii) In the Y (South) direction, however, the models are statistically equivalent in terms of explanatory metrics (R^2, Adjusted R^2, NSE; $p \approx 1.000$) and MSE/RMSE ($p \geq 0.934$); significant differences are observed only in KGE ($p = 0.012$, in favor of the linear form) and MAE ($p < 0.001$), while MAPE remains borderline ($p = 0.073$). (iii) Training–validation (generalization gap) comparisons are largely insignificant; the few significant cases include the MAPE of the linear model in the X direction ($p = 0.008$), the MAPE of the linear model in the Y direction ($p = 0.035$), and the KGE of the logarithmic model in both directions ($p < 0.001$); and the latter indicates the sensitivity of the logarithmic form's KGE component balance to the transition from training to validation.

When Figures 5 and 6 are evaluated together, it is clearly evident that the model-form selection for the X (West) and Y (South) components of the Burdur Lake LSA centroid cumulative displacement is direction dependent. In the X (West) direction, the OLS-logarithmic model produced higher validation means/lower validation errors in both explanatory-based metrics (R^2, Adjusted R^2, NSE) and error-based metrics (MAE, MAPE, MSE, RMSE); this superiority is not limited to visual/mean comparisons but is also supported by Wilcoxon matched-pairs test results. Indeed, in the X (West) panels in Figure 7, the validation(linear)–validation(logarithmic) comparisons showed statistically significant differences at the $p < 0.001$ level across multiple metrics. Thus, it has been confirmed that the gain provided by the logarithmic form in the X component is not "random" within the MCCV uncertainty but is statistically strongly differentiated. Therefore, in forward simulation and prediction steps, it would be more meaningful and statistically more accurate to model and base the X (West) component using the logarithmic form.

Figure 7. Two-sided matched Wilcoxon signed-rank test p-value matrices for the MCCV-based comparison of OLS-linear and OLS-logarithmic models in direction-based experiments and optimization criteria. (Note: This figure summarizes the statistical significance of the differences between the performance metrics produced by OLS-linear and OLS-logarithmic models over 15 Monte Carlo cross-validation (MCCV) iterations using a two-sided matched Wilcoxon signed-rank test. Since the metrics produced in the same MCCV iteration were matched step-by-step, comparisons were made in a matched-pairs (paired) arrangement, with n = 15 matched observations for each pairwise comparison. Each subpanel displays the pairwise p-values between the four matched conditions (Linear-Train, Linear-Validation, Logarithmic-Train, Logarithmic-Validation) for the relevant metric in a lower-triangular heatmap format (diagonal cells are defined as $p = 1.000$). The color scale encodes the magnitude of the p-value (darker shades indicate smaller p-values and stronger evidence against

the null hypothesis); values reported as $p = 0.000$ correspond to $p < 0.001$ due to rounding. The panels are organized based on (i) direction and (ii) success criteria: (West)-Maximization (**a**–**d**), X (West)-Minimization (**e**–**h**), Y (South)-Maximization (**i**–**l**), and Y (South)-Minimization (**m**–**p**). Maximization-based metrics include R^2 (**a**,**i**), Adjusted R^2 (**b**,**j**), NSE (**c**,**k**), and KGE (**d**,**l**); minimization-based metrics include MAE (**e**,**m**), MAPE (**f**,**n**), MSE (**g**,**o**), and RMSE (**h**,**p**). The pairwise comparisons in the subpanels serve three main purposes: (1) Train-Validation difference in the linear model (generalization gap/overfitting signal), (2) Train-Validation difference in the logarithmic model, and (3) Validation difference between models (statistical divergence in validation performance). A significance threshold of $\alpha = 0.05$ was used (two-tailed test).

In contrast, in the Y (South) direction, while Figure 6 shows that the linear model offers a more advantageous profile on mean in metrics such as R^2/NSE and KGE, the Wilcoxon matrices in Figure 7 require a more cautious interpretation of the evidence regarding the model form in the Y direction. For Y (South), validation(linear)–validation(logarithmic) comparisons did not produce a meaningful difference in many metrics (particularly in explanatory-based metrics such as R^2, Adjusted R^2, and NSE, where p-values were close to 1.000, indicating that the divergence was lost within the MCCV iterations). This finding indicates that the validation performance of the two models in the Y component remains largely statistically equivalent, thus not strongly supporting the claim of a "clear superiority" across many metrics. However, in modeling practice, not only statistical significance but also the direction of mean validation success, the magnitude of the generalization gap, and the joint consistency of metrics are considered. In this context, since the linear model shows a tendency for more balanced/superior performance at the mean level in the Y (South) component and, in particular, offers a better profile in KGE, which is a balancing fit measure, the approach of treating the Y component with a linear form in subsequent simulation stages emerges as a more appropriate choice.

3.4. 2026–2035 Projections

Figure 8 is the key output that visually demonstrates the extent to which projections made for the 2026–2035 horizon remain stable under MCCV-based sampling randomness. Although the logarithmic form was found to be stronger in terms of both mean performance and Wilcoxon matched-pairs test results in the X (West) direction in previous sections, the model selection was component-based due to the mean performance favoring the linear form in the Y (South) direction, despite no statistically significant difference being observed (see Figure 7). Nevertheless, regardless of this choice, all four basic models were projected within the same framework for 2026–2035. In each panel, the full-fit curve, 15 separate Monte Carlo projections generated with 15 MCCV coefficients, and the MC-Mean projection obtained from the mean of these coefficients are presented together for the same forecast horizon. The fact that the curves in all panels Figure 8a–d are very close to each other and maintain almost the same angular trend (parallel trend behavior) indicates that the coefficients remain stable throughout the MCCV and that the projection is not overly sensitive to a single split. Additionally, the fact that the upper and lower prediction interval (PI) limits given at the $\alpha = 0.05$ level form a similarly narrow and regular band across all four panels indicates that uncertainty remains manageable when projected to the 2026–2035 horizon. The β_0 and β_1 coefficients, which are the parametric source of this consistency, are also reported in Table 1 in a traceable manner based on MCCV steps. The absence of outliers in the coefficient distributions and the balanced structure of the medians/quartiles, supported by Figure 5, reinforce the methodological reliability of the projections.

https://doi.org/10.3390/atmos17080710

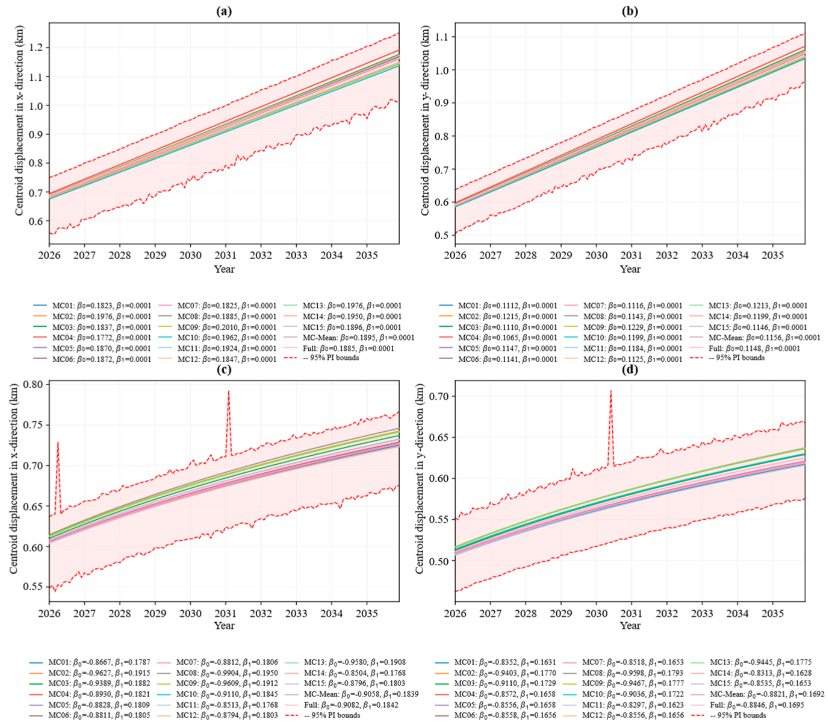

Figure 8. Comparison of 2026–2035 projections under MCCV uncertainty (n = 15): Full-fit, 15 Monte Carlo (MCCV) projections, and MC-Mean projection for OLS-linear and OLS-logarithmic trend forms in the X (West) and Y (South) components, along with 95% PI (α = 0.05). Panels: (**a**) X-linear, (**b**) X-logarithmic, (**c**) Y-linear, (**d**) Y-logarithmic. Each panel shows 17 forecast curves (15 MC + 1 MC-Mean + 1 Full-fit) for the 2026–2035 horizon. All projection curves are anchored to the most recent observed centroid position; this shift correction does not alter the estimated trend coefficients or the statistical results.

Figure 9a. This figure shows the cross-scenario where the OLS-linear components for X (West) and Y (South) are used together (Figure 8a,c). (Note: This combination should be interpreted as a "reference/alternative" scenario because it imposes a linear form on both axes: Considering that the logarithmic form in the X direction is evident both in mean performance and in Wilcoxon comparisons (Figure 6), even if the projection bundle in panel (a) is "consistent and parallel," it is a secondary scenario in terms of representing the model-form preference in the X component. However, the narrow and closely spaced bands indicate that the MCCV coefficients (Table 1) remain stable under sampling randomness and that the spatial projection is geometrically controlled.)

Figure 9b. This is the most expected scenario, combining the OLS-logarithmic component for X (West) and the OLS-linear component for Y (South) (defined as the target scenario matching Figure 8b,c). This panel represents the most consistent combination based on model selection rationale. The logarithmic form in X produces meaningful and robust improvements in validation metrics. The linear form in Y maintains superior mean performance and provides a more balanced profile than the logarithmic form in many metrics (see Figure 6). Furthermore, the fact that the form difference in the Y direction does not become statistically significant in most metrics (Figure 7) makes the linear selection risk-minimizing. Consequently, the panel in Figure 9b can be reported as the main scenario from both a methodological (statistical evidence) and practical (mean superiority and stability) perspective.

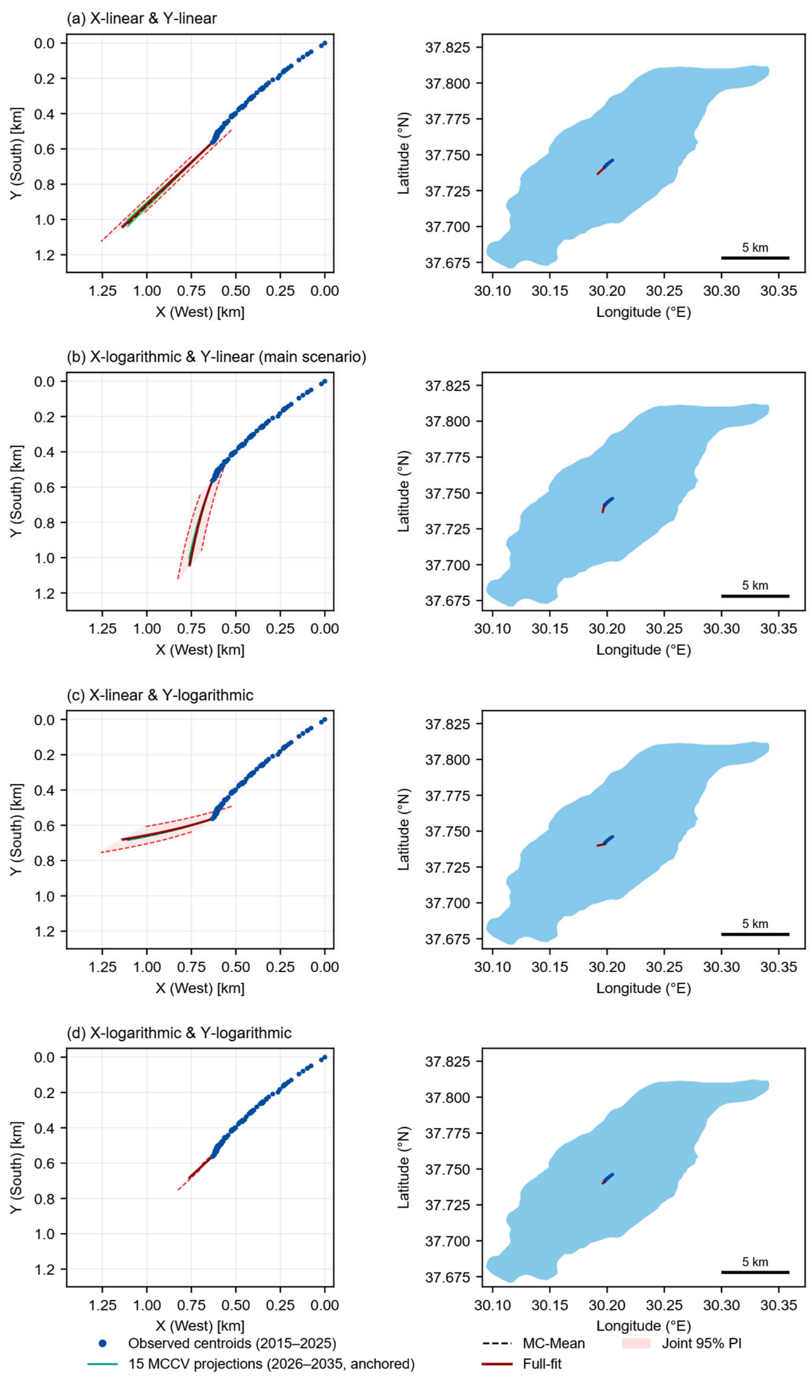

Figure 9. Spatial representation of 2 × 2 cross-trend scenarios under the 2026–2035 projections: The addition of Monte Carlo-based joint prediction intervals (joint PI, 95%) generated by four combinations of OLS-linear and OLS-logarithmic trend forms for the X (West) and Y (South) components onto the observed (2015–2025) centroid points. A total of 17 × 17 = 289 projection curves (15 MCCV coefficient sets + MC-Mean + full-fit for each direction) for a single scenario in each panel were evaluated together, and the pattern consistency and geometric projection of near-future scenarios (2026–2035) were visualized. The meaningful separation of the logarithmic form in the X direction is supported by the matched comparisons in Figure 6, while the lack of statistical significance of the linear–logarithmic difference in the Y direction for most metrics (Figure 6) was referenced in the scenario interpretations. The panels correspond to the following combinations of trend forms: (**a**) X-linear and Y-linear, (**b**) X-logarithmic and Y-linear, (**c**) X-linear and Y-logarithmic, and (**d**) X-logarithmic

and Y-logarithmic. All projection curves are anchored to the most recent observed centroid position; this shift correction does not alter the estimated trend coefficients or the statistical results.

Figure 9c. It presents the unexpected/reverse scenario where the OLS-linear component for X (West) and the OLS-logarithmic component for Y (South) are combined (Figure 8a,d). This combination is particularly important for testing model-form sensitivity, as it contradicts the prominence of the logarithmic form in the X component (Figure 6). The projection bundle remains tight and parallel, indicating that the trend direction does not change under uncertainty; however, it suggests linearization in the X component for optimal form selection. The selection of the logarithmic form in the Y component remains a possible alternative, as the statistical distinction in Y is not confirmed for most metrics (see Figure 7); however, since the mean performance superiority is linear (see Figure 6), the panel in Figure 9c should be positioned as a sensitivity scenario rather than the main scenario.

Figure 9d. This is the full-logarithmic scenario using the OLS-logarithmic components for X (West) and Y (South) together (Figure 8b,d). This choice is consistent with both mean performance and statistical divergence for the X direction (Figure 7); therefore, panel (d) of Figure 9 has a strong basis for the X component. For the Y direction, although the log form is competitive in some error metrics (see Figure 6), it does not consistently show statistical superiority in most measures (see Figure 7); therefore, the panel in Figure 9d is reported as a possible but secondary scenario. Nevertheless, the consistent bundle behavior of the entire logarithmic scenario is an important control output, highlighting that the MCCV coefficients (see Table 1) and coefficient stability (distributional consistency in Figure 5) are successfully transferred to the projection geometry.

At this point, the limitations of the projections must be clearly stated. The 2026–2035 projections are extrapolations based on a single observation window of approximately ten years and rely on the assumption that the trend pattern (stability) will persist into the future. The reported forecast ranges reflect only coefficient (sampling) uncertainty; they do not account for potential changes in climate regimes, disruptions in groundwater use and water management policies, exceptionally dry or wet years, or structural uncertainties inherent in the model itself. Therefore, the presented ranges should be interpreted not as a definitive forecast of the future, but within the framework of scenario continuity—that is, "assuming the current trend continues"; the validity of this assumption naturally weakens as the projection horizon extends.

4. Discussion and Conclusions

In this study, changes in the surface area of Lake Burdur during the 2015–2025 period and the resulting directional movement of the lake's geometric center were analyzed using Sentinel-2 L2A satellite imagery. Monthly lake surface area masks were obtained using a fixed study window, a lake vicinity mask, and unsupervised K-means clustering with three classes; subsequently, centroid locations were calculated from these masks to model the cumulative displacement components in the West and South directions. In this regard, the study provides a more interpretable monitoring framework that explains not only the shrinkage of the lake area but also the spatial direction in which the shrinkage is concentrated.

The findings indicate that the centroid movement in Lake Burdur exhibits different trend structures depending on the direction. In the X/West direction, the OLS-logarithmic model produced higher validation success and lower error compared to the linear model in terms of R^2, Adjusted R^2, NSE, and error metrics. Wilcoxon paired comparison results also showed that this difference was statistically significant across many metrics. In contrast, in the Y/South direction, the linear model offered a more balanced performance, particularly in terms of mean validation success and the KGE metric; although the logarithmic model was competitive in some error metrics, the linear form was found to be more appropriate for overall model selection. This result indicates that lake shrinkage does not exhibit the same uniform geometric behavior as the horizontal and vertical directional components.

The 2026–2035 projections have yielded significant results regarding the incorporation of MCCV-based parameter uncertainty into forward-looking spatial scenarios. The fact that the projection curves obtained under different model combinations form closely spaced and regular bands indicates that the model parameters are robust to sampling uncertainty. In particular, the scenario using a logarithmic model in the X direction and a linear model in the Y direction can be considered the most consistent main scenario in terms of both statistical evidence and mean performance metrics. This finding suggests that the centroid movement in Lake Burdur may exhibit a controlled yet ongoing spatial shift trend in the coming years.

When evaluated in conjunction with the literature on watersheds, the likely drivers of the observed loss of area and centroid shift can be grouped under three main headings. First, within the natural variability of the semi-arid Mediterranean climate, there is an increase in evaporation and reference evapotranspiration (ET_0) driven by precipitation deficits and rising temperatures; due to its closed-basin nature, Lake Burdur's water budget is directly and unmitigatedly sensitive to atmospheric water loss [19,20]. Second, the widespread use of groundwater extraction and agricultural irrigation in the basin: these anthropogenic interventions reduce both the surface runoff reaching the lake and the groundwater component that feeds it [19,20]. Third, the lake's bottom topography: since shrinkage leads to the drying up of larger areas in sections with shallow shoreline flats, the west–southward movement of the centroid is consistent with the relatively rapid drying of shallow areas in the opposite (northeast) sections of the lake; however, this interpretation requires verification through bathymetric data and shoreline analyses. It should be strongly emphasized that, since the trend models in this study are established solely based on time, the assessments of drivers presented here do not constitute causal inferences but rather a qualitative association grounded in the literature.

Figure 10 presents the time series of lake surface area (LSA) derived from a 111-month water mask. The surface area, which was 136.82 km^2 in September 2015, had decreased to 117.06 km^2 by November 2025; a significant loss of 19.76 km^2 (14.4%) occurred over the 10.16-year observation period. The OLS-linear trend indicates a remarkably stable rate of shrinkage of −1.80 km^2/year (R^2 = 0.979). This stability suggests that the loss reflects the cumulative effect of a persistent atmospheric forcing—evaporative demand (ET_0) driven by a precipitation deficit and rising temperatures—rather than isolated drought events; under closed-basin conditions, this monotonous decrease in surface area can be interpreted as a direct surface signature of the disruption in the climate–evaporation balance [19,20,22]. The fact that seasonal fluctuations remain within a narrow band around the trend line also supports the high signal-to-noise ratio and the dominant role of atmospheric water budget components.

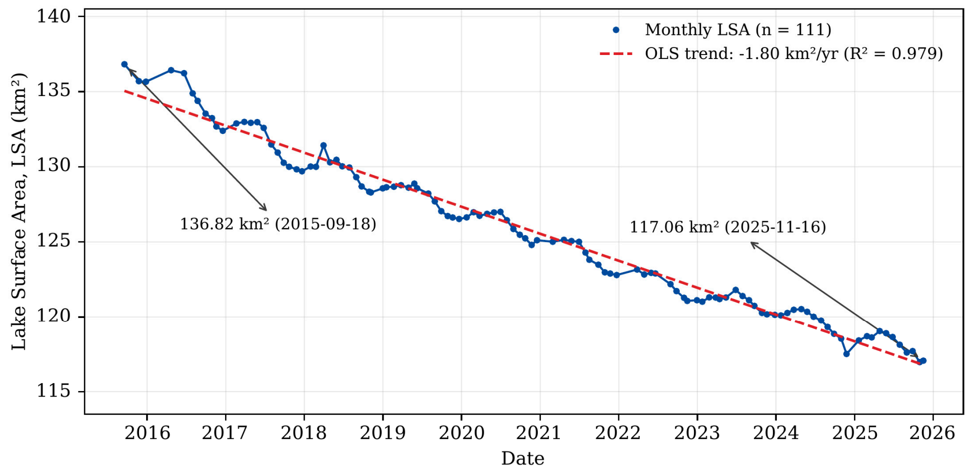

Figure 10. A monthly time series of the surface area (LSA) of Lake Burdur derived from Sentinel-2 data (September 2015-November 2025, n = 111) and the OLS-linear trend (−1.80 km^2/year; R^2 = 0.979). The starting and ending values are marked on the graph.

The practical benefit of centroid tracking can also be justified within this framework: while the area series indicates "how much" the lake has shrunk, centroid kinematics summarizes "where and in which direction" the shrinkage is concentrated, providing a compact vector indicator that cannot be derived from the area series alone. This directional information provides a low-cost early-warning indicator for monitoring and prioritizing areas at risk of dust/salt aerosol emissions from drying lake beds, ecologically critical shallow habitats, and shoreline uses.

In semi-arid closed basins, lake surface area is both a result and a component of atmosphere–surface interactions: (i) in closed lakes, atmospheric evaporation is the dominant loss term in the water budget, and the shrinkage observed in the area series serves as an integrated surface indicator of both regional precipitation deficits and increasing evaporative demand; (ii) a shrinking water surface feeds back into micro- and mesoscale atmospheric conditions by altering local humidity, temperature, and lake breeze regimes; and (iii) drying salt lake beds have the potential to become a source of atmospheric dust and salt aerosols, as documented in the Aral Sea case [3,4,32]. Therefore, the Sentinel-2-based area and centroid monitoring framework is positioned as an observational infrastructure that provides consistent long-term observations of lake surface dynamics.

In conclusion, this study demonstrates that changes in surface area in lakes characterized by semi-arid and closed-basin conditions can be monitored not only through spatial extent but also through centroid kinematics. In the case of Lake Burdur, the proposed approach combines remote sensing, unsupervised segmentation, directional trend modeling, and Monte Carlo cross-validation to provide a more robust explanation of the spatial characteristics of lake shrinkage. However, the study's limitations include cloud cover in satellite images, the sensitivity of segmentation class interpretations to image quality, and the fact that trend models were established solely on a time-dependent basis. In future studies, incorporating hydro-climatic and anthropogenic variables such as precipitation, temperature, evaporation, groundwater use, and agricultural irrigation into the model will contribute to a more comprehensive explanation of the cause-and-effect relationships underlying the drawdown dynamics of Lake Burdur. However, all 111 water masks used in the analysis, along with their centroid locations and the reference contour dated 18 September 2015, are presented in Appendix C; this comprehensive visual inspection confirmed that the masks contained no cloud-induced gaps or discontinuities, that the centroid progression was regular, and that the water mass did not reach the boundary of the fixed working window on any date.

To these limitations, we must also add the fact that segmentation accuracy could not be quantitatively assessed using an independent reference dataset. Since there were no field measurements taken simultaneously with the coastline during the study period, nor a consistent, higher-resolution reference dataset spanning the study dates, a formal accuracy assessment using an error matrix or Kappa coefficient could not be performed; this is a clear limitation of the study. However, three indirect quality indicators support the reliability of the results: (i) a visual inspection of all 111 masks presented in Appendix C revealed no cloud-induced gaps, discontinuities, or classification fragmentation; (ii) the centroid and area time series progress steadily without sudden jumps, which are typical signs of classification errors; and (iii) the low dispersion of the area series around its linear trend (R^2 = 0.979) indicates intra-series consistency. A cross-validation with the "water" class in the Scene Classification Layer of L2A products is planned as a means of partial independent validation in future studies.

Author Contributions: Conceptualization, M.G., N.O.Ü., D.Y. (Doğan Yıldız) and D.Y. (Dursun Yıldız); methodology, M.G. and N.O.Ü.; software, M.G.; validation, M.G., N.O.Ü., D.Y. (Doğan Yıldız) and D.Y. (Dursun Yıldız); formal analysis, M.G. and N.O.Ü.; investigation, M.G. and N.O.Ü.; resources, M.G. and N.O.Ü.; data curation, M.G. and N.O.Ü.; writing—original draft preparation, M.G. and N.O.Ü.; writing—review and editing, D.Y. (Doğan Yıldız) and D.Y. (Dursun Yıldız); visualization, M.G. and N.O.Ü.; supervision, D.Y. (Doğan Yıldız) and D.Y. (Dursun Yıldız); project administration, M.G. and N.O.Ü. All authors have read and agreed to the published version of the manuscript.

Funding: This research received no external funding.

Data Availability Statement: The satellite imagery used in this study was obtained from publicly available Copernicus Sentinel-2 Level-2A products. The processed data generated during the study are available from the corresponding author upon reasonable request.

Acknowledgments: The authors would like to thank the Copernicus Programme for providing open-access Sentinel-2 satellite imagery used in this study.

Conflicts of Interest: The authors declare no conflicts of interest.

Abbreviations

LSA	Lake Surface Area
OLS	Ordinary Least Squares
MCCV	Monte Carlo Cross-Validation
CV	Cross-Validation
NSE	Nash–Sutcliffe Efficiency
KGE	Kling–Gupta Efficiency
MAE	Mean Absolute Error
MAPE	Mean Absolute Percentage Error
MSE	Mean Squared Error
RMSE	Root Mean Square Error
PI	Prediction Interval
N	North
NE	Northeast
E	East
SE	Southeast
S	South
SW	Southwest
W	West
NW	Northwest

Appendix A

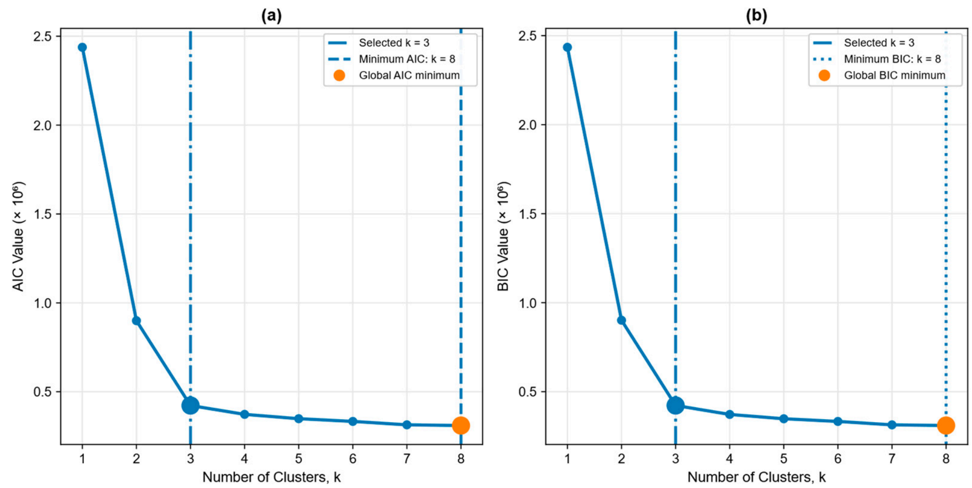

Figure A1. AIC and BIC diagnostic plots for determining the number of clusters in the K-Means algorithm. Panel (**a**) shows the variation in AIC values as a function of the number of clusters, while panel (**b**) shows the variation in BIC values as a function of the number of clusters. In both panels, the minimum values are obtained at k = 8, although the most pronounced decrease occurs between k = 1 and k = 3. After k = 3, the improvement in the curves becomes more limited. This suggests that clusters beyond the third represent nuances in hue and intensity within existing classes rather than forming new main surface classes. Therefore, considering both model simplicity and physical interpretability, the number of clusters for the K-Means algorithm was selected as k = 3. In both panels, the orange marker denotes the global minimum of the corresponding information criterion (k = 8), while the vertical dashed lines mark this minimum and the selected number of clusters (k = 3). (k = n_cluster parameter).

Appendix B

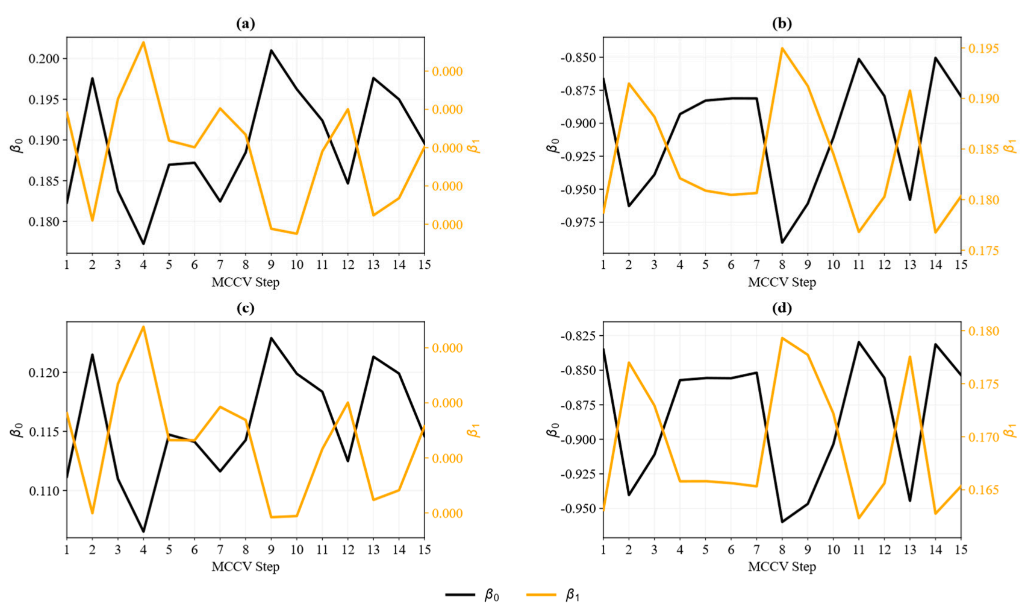

Figure A2. Model-based β distribution summary (X-linear, X-logarithmic, Y-linear, Y-logarithmic); Here, the coefficient distributions of (**a**) X (West) linear, (**b**) X (West) logarithmic, (**c**) Y (South) linear, and (**d**) Y (South) logarithmic models are presented in a more compact form, supporting the findings in Table 1 and Figure 5 of the main text with a complementary visual summary.

Appendix C

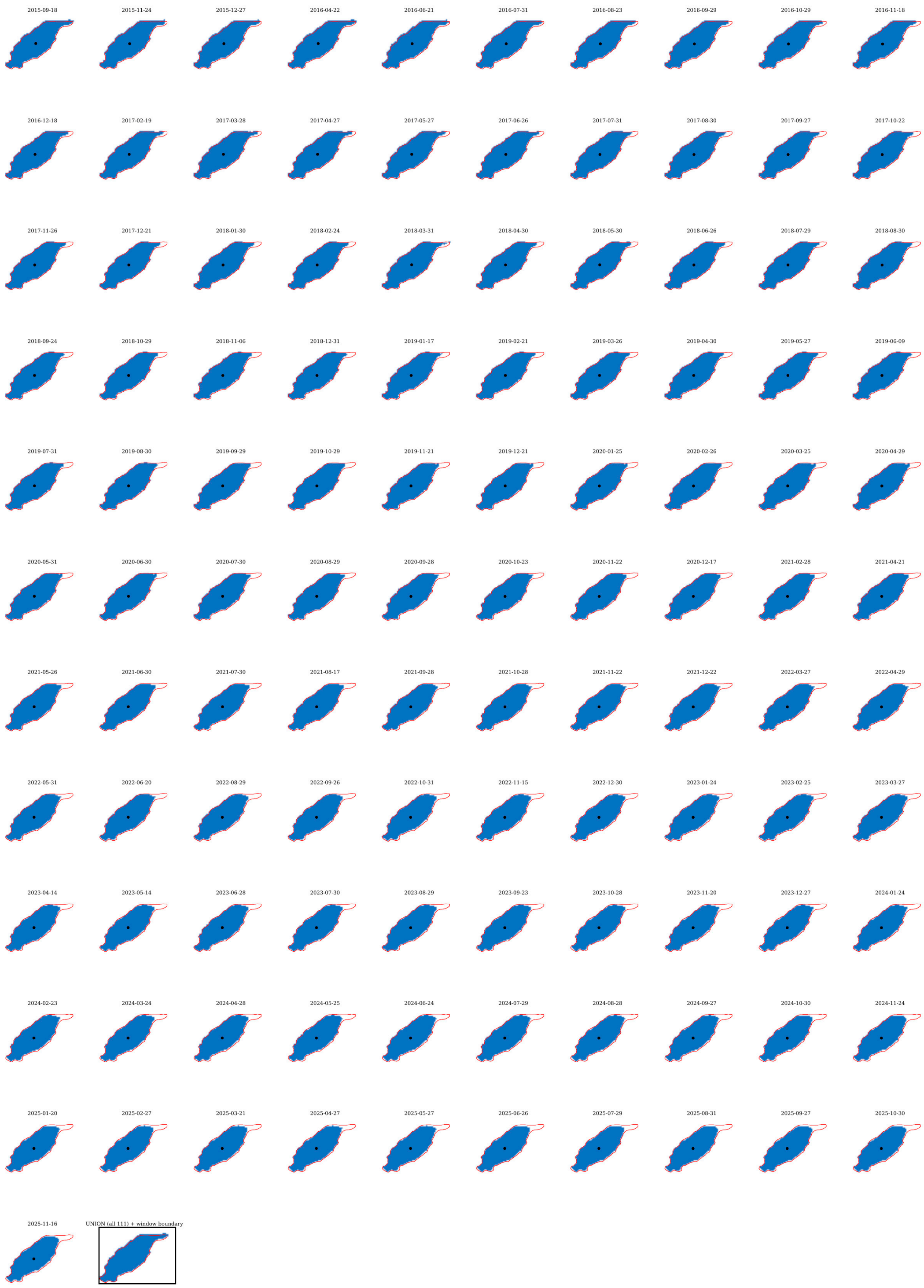

Figure A3. The fixed study window boundary based on the union of all 111 monthly dual-water masks for the 2015–2025 period and (the last panel) the union of the 111 masks. Each panel shows the centroid location (black dot) for the corresponding date and the reference lake contour (red) as of 18 September 2015. It can be seen that none of the masks contain cloud-induced gaps or discontinuities, the centroid progression is regular, and the water body does not reach the window boundary on any date.

References

1. Pekel, J.-F.; Cottam, A.; Gorelick, N.; Belward, A.S. High-resolution mapping of global surface water and its long-term changes. *Nature* **2016**, *540*, 418–422. https://doi.org/10.1038/nature20584.
2. Pi, X.; Luo, Q.; Feng, L.; Xu, Y.; Tang, J.; Liang, X.; Bryan, B.A. Mapping global lake dynamics reveals the emerging roles of small lakes. *Nat. Commun.* **2022**, *13*, 5777. https://doi.org/10.1038/s41467-022-33239-3.
3. Yang, X.; Wang, N.; Chen, A.; He, J. Changes in area and water volume of the Aral Sea in the arid Central Asia over 1960–2018 and their causes. *Catena* **2020**, *195*, 104566. https://doi.org/10.1016/j.catena.2020.104566.
4. AghaKouchak, A.; Norouzi, H.; Madani, K.; Mirchi, A.; Azarderakhsh, M.; Nazemi, A.; Hassanzadeh, E. Aral Sea syndrome desiccates Lake Urmia: Call for action. *J. Gt. Lakes Res.* **2015**, *41*, 307–311. https://doi.org/10.1016/j.jglr.2014.12.007.
5. Shugar, D.H.; Burr, A.; Haritashya, U.K.; Kargel, J.S.; Watson, C.S.; Kennedy, M.C.; Clague, J.J. Rapid worldwide growth of glacial lakes since 1990. *Nat. Clim. Change* **2020**, *10*, 939–945. https://doi.org/10.1038/s41558-020-0855-4.
6. Drusch, M.; Del Bello, U.; Carlier, S.; Colin, O.; Fernandez, V.; Gascon, F.; Meygret, A. Sentinel-2: ESA�s optical high-resolution mission for GMES operational services. *Remote Sens. Environ.* **2012**, *120*, 25–36. https://doi.org/10.1016/j.rse.2011.11.026.
7. Fu, M.; Zheng, Y.; Qian, C.; He, Q.; He, Y.; Wei, C.; Yang, K.; Zhao, W. Spatiotemporal evolution and driving mechanism analysis of Dongting Lake based on multi-source remote sensing data. *Ecol. Inform.* **2024**, *83*, 102822. https://doi.org/10.1016/j.ecoinf.2024.102822.
8. Song, W.; Hu, Q.; Liu, S.; Hou, Y. Spatiotemporal evolution and driving factor analysis of water bodies in Zhengzhou City based on Google Earth Engine platform. *Sci. Rep.* **2025**, *15*, 45089. https://doi.org/10.1038/s41598-025-32480-2.
9. Zi, F.; Wang, Y.; Lu, S.; Ikhumhen, H.O.; Fang, C.; Li, X.; Wang, N.; Kuang, X. Changes in the Water Area of an Inland River Terminal Lake (Taitma Lake) Driven by Climate Change and Human Activities, 2017–2022. *Remote Sens.* **2024**, *16*, 1703. https://doi.org/10.3390/rs16101703.
10. Policelli, F.; Hubbard, A.; Jung, H.C.; Zaitchik, B.F.; Ichoku, C. Lake Chad total surface water area as derived from land surface temperature and radar remote sensing data. *Remote Sens.* **2018**, *10*, 252. https://doi.org/10.3390/rs10020252.
11. Zuo, J.; Jiang, W.; Li, Q.; Du, Y. Remote sensing dynamic monitoring of the flood season area of Poyang Lake over the past two decades. *Nat. Hazards Res.* **2024**, *4*, 8–19. https://doi.org/10.1016/j.nhres.2023.12.017.
12. Song, W.; Huang, T.; You, Q.; Zhang, Y.; Zhao, K.; Zhang, H.; Wang, Y.; Li, X. Spatiotemporal dynamics and driving forces of the typical plateau and plain lakes in China based on Google Earth Engine. *Front. Environ. Sci.* **2024**, *12*, 1365972. https://doi.org/10.3389/fenvs.2024.1365972.
13. Jiang, W.; Zhou, F.; Hu, C.; Lin, X.; Zhang, D. Profiling the dynamics of Tonle Sap Lake, Cambodia. *Sci. Total Environ.* **2024**, *933*, 170444. https://doi.org/10.1016/j.scitotenv.2024.170444.
14. Danesh-Yazdi, M.; Bayati, M.; Tajrishy, M.; Chehrenegar, B. Revisiting bathymetry dynamics in Lake Urmia using extensive field data and high-resolution satellite imagery. *J. Hydrol.* **2021**, *603*, 126987. https://doi.org/10.1016/j.jhydrol.2021.126987.
15. Coe, M.T.; Foley, J.A. Remote sensing of Lake Chad: Basin-scale approach to monitoring seasonal and interannual water changes. *R. Soc. Open Sci.* **2017**, *4*, 171120. https://doi.org/10.1098/rsos.171120.
16. Huang, S.; Chen, X.; Ma, X.; Fang, H.; Liu, T.; Kurban, A.; Guo, J.; De Maeyer, P.; Van de Voorde, T. Monitoring Surface Water Area Changes in the Aral Sea Basin Using the Google Earth Engine Cloud Platform. *Water* **2023**, *15*, 1729. https://doi.org/10.3390/w15091729.
17. Durdiev, D.; Abduraxmonov, A.; Khasankhonov, K. Land cover change detection in the Aralkum with multisource satellite datasets. *GISci. Remote Sens.* **2022**, *59*, 17–35. https://doi.org/10.1080/15481603.2021.2009232.
18. Huth 2022; Gessner, J.; Klein, U.; Yesou, I.; Lai, H.; Oppelt, X.; N.; Kuenzer, C. Analyzing Water Dynamics Based on Sentinel-1 Time Series-a Study for Dongting Lake Wetlands in China. *Remote Sens.* **2020**, *12*, 1761. https://doi.org/10.3390/rs12111761.
19. Şener, Ş.; Şener, E.; Davraz, A.; Varol, S. Hydrogeological and hydrochemical investigation in the Burdur Saline Lake Basin, southwest Turkey. *Geochemistry* **2020**, *80*, 125592. https://doi.org/10.1016/j.chemer.2019.125592.
20. Çolak, M.A.; Öztaş, B.; Özgencil, İ.K.; Soyluer, M.; Korkmaz, M.; Ramírez-García, A.; Metin, M.; Yılmaz, G.; Ertuğrul, S.; Tavşanoğlu, Ü.N.; et al. Increased Water Abstraction and Climate Change Have Substantial Effect on Morphometry, Salinity, and Biotic Communities in Lakes: Examples from the Semi-Arid Burdur Basin (Turkey). *Water* **2022**, *14*, 1241. https://doi.org/10.3390/w14081241.

21. Albarqouni, M.M.Y.; Yagmur, N.; Balcik, F.B.; Sekertekin, A. Assessment of Spatio-Temporal Changes in Water Surface Extents and Lake Surface Temperatures Using Google Earth Engine for Lakes Region, Türkiye. *ISPRS Int. J. Geo-Inf.* **2022**, *11*, 407. https://doi.org/10.3390/ijgi11070407.
22. Yao, F.; Livneh, B.; Rajagopalan, B.; Wang, J.; Crétaux, J.-F.; Wada, Y.; Berge-Nguyen, M. Satellites reveal widespread decline in global lake water storage. *Science* **2023**, *380*, 743–749. https://doi.org/10.1126/science.abo2812.
23. Hartigan, J.A.; Wong, M.A. Algorithm AS 136: A K-means clustering algorithm. *J. R. Stat. Soc. Ser. C* **1979**, *28*, 100–108. https://doi.org/10.2307/2346830.
24. Akaike, H. A new look at the statistical model identification. *IEEE Trans. Autom. Control* **1974**, *19*, 716–723. https://doi.org/10.1109/TAC.1974.1100705.
25. Schwarz, G. Estimating the dimension of a model. *Ann. Stat.* **1978**, *6*, 461–464. https://doi.org/10.1214/aos/1176344136.
26. McFeeters, S.K. The use of the Normalized Difference Water Index (NDWI) in the delineation of open water features. *Int. J. Remote Sens.* **1996**, *17*, 1425–1432. https://doi.org/10.1080/01431169608948714.
27. Xu, H. Modification of normalised difference water index (NDWI) to enhance open water features in remotely sensed imagery. *Int. J. Remote Sens.* **2006**, *27*, 3025–3033. https://doi.org/10.1080/01431160600589179.
28. Xu, Q.-S.; Liang, Y.-Z. Monte Carlo cross validation. *Chemom. Intell. Lab. Syst.* **2001**, *56*, 1–11. https://doi.org/10.1016/S0169-7439(00)00122-2.
29. Nash, J.E.; Sutcliffe, J.V. River flow forecasting through conceptual models part I—A discussion of principles. *J. Hydrol.* **1970**, *10*, 282–290. https://doi.org/10.1016/0022-1694(70)90255-6.
30. Gupta, H.V.; Kling, H.; Yilmaz, K.K.; Martinez, G.F. Decomposition of the mean squared error and NSE performance criteria: Implications for improving hydrological modelling. *J. Hydrol.* **2009**, *377*, 80–91. https://doi.org/10.1016/j.jhydrol.2009.08.003.
31. Wilcoxon, F. Individual comparisons by ranking methods. *Biom. Bull.* **1945**, *1*, 80–83. https://doi.org/10.2307/3001968.
32. Indoitu, R.; Kozhoridze, G.; Batyrbaeva, M.; Vitkovskaya, I.; Orlovsky, N.; Blumberg, D.; Orlovsky, L. Dust emission and environmental changes in the dried bottom of the Aral Sea. *Aeolian Res.* **2015**, *17*, 101–115. https://doi.org/10.1016/j.aeolia.2015.02.004.